Advanced Magnetoresistive Sensors for Industrial Applications

Tiago Costa

tscosta94@gmail.com

Instituto Superior Técnico, Lisboa, Portugal

October 2017

Abstract

Advanced MR sensors - the magnetic tunnel junctions - were implemented in a system alongside magnets aimed to magnetize and read MI patterns. The development of this system was done in two main stages. First the search for the best magnet-sensor configuration using both simulation with finite element modeling (FEM) and measurements. Then the validation of different sensor array configurations. This validation was done through measurements of well-defined structures of a hard ferromagnetic alloy, micro-fabricated in a clean-room environment, and comparison with a 2D simulation.

Keywords: Magnetic tunnel junctions, Magnetic ink, Magnetic encoder, Stray field measurement, Magnetic field simulation

1. Introduction

Metrology and accurate positioning is of major relevance for industry. Nowadays there is competitive demand for small size devices with the lowest cost possible and capable of performing even in harsh environments. Currently, the most widespread used technology is optical detection, which allow high accuracy, resolution and reliability. However, in harsh environments such systems become bigger, more expensive and more fragile. Precision encoding can therefore benefit from the use of magnetic technology.

Magnetic encoder systems are capable of converting mechanical rotational or linear movement into an analog or digital signal using magnetic technology. They are comprised of a reading head and a track that encodes the position through the creation of stray magnetic fields. Nowadays the most widely used magnetic sensing technology used is hall-effect based [10]. However, other magnetic technologies, and in particular magnetoresistance (MR) based, offer clear advantages when compared to optical detection and also to the other magnetic technologies. MR sensors - in particular state of the art Magnetic Tunnel Junctions (MTJs) - can be produced in micrometic dimensions at massive scale, at low cost and capable of high sensitivity to weak magnetic fields [7, 9].

State-of-the-art magnetic tracks for positioning systems, such as the ones produced by Bogen Electronic GmbH are hard magnetic and made of an elastomer filled with ferrite [1]. Fabricating tracks with Magnetic Ink allows a great improvement both in cost and complexity of the production. The use of magnetic ink is already widely used for security purposes such as banknotes and checks, such as using Magnetic Ink Character Recognition (or MICR) [8]. However, for positioning applications there is still development to be made.

This work is done in the scope of the project GePos, a partnership between INESC-MN and Bogen Electronic GmbH, that a precise magnetic encoder system using magnetoresistance technology and in particular state-of-the-art MTJs. The main objective of the project is the development of a system capable of measuring positions using magnetic ink, allowing a higher versatility in today's industry applications. This work is focused on the development of the reading head with the goal of measuring patterns printed with magnetic ink.

2. Theoretical Background

2.1. Magnetostatics and Magnetic Materials

The magnetic **H**-field is an indispensible auxiliary field when dealing with magnetic materials . The magnetization of a solid reflects the local value of **H** [5, 3]. In free space, both the **B** and **H** are related by the magnetic permeability μ_0 as $\mathbf{B} = \mu_0\mathbf{H}$. Therefore, in free space, the derivation of both fields is interchangeable and immediate. In magnetic materials however, the **H**-field relates to the **B**-field through the constitutive relation:

$$\mathbf{H} = \frac{\mathbf{B}}{\mu_0} - \mathbf{M}, \qquad (1)$$

where $\mathbf{M}$ is the magnetization. This field is not divergenceless ($\nabla \cdot \mathbf{H} = -\nabla \cdot \mathbf{M}$), so comparing with the electric field, a calculation of this field can be done by considering the existence of fictitious magnetic charges, both in the bulk $\rho_m = -\nabla \cdot \mathbf{M}$ and on the surface $\sigma_m = \mathbf{M} \cdot \mathbf{e}_n$. So the stray field can be integrated using the relation:

$$
\begin{aligned}
\mathbf{H}(\mathbf{r}) = & -\frac{1}{4\pi} \int_V d^3 r' \left(\nabla \cdot \mathbf{M}(\mathbf{r}') \right) \frac{\mathbf{r} - \mathbf{r}'}{|\mathbf{r} - \mathbf{r}'|^3} \\
& + \frac{1}{4\pi} \int_S d^2 r' \left(\mathbf{M}(\mathbf{r}') \cdot \mathbf{e}_n \right) \frac{\mathbf{r} - \mathbf{r}'}{|\mathbf{r} - \mathbf{r}'|^3},
\end{aligned}
\tag{2}
$$

where the integration for the bulk charges is made on the bulk volume V, and the surface charges on the charged surface S, where $\mathbf{r}'$ is the position vector of the fictitious charge and $\mathbf{r}$ the position vector where the field is calculated.

There are four main classifications for magnetic materials: diamagnetic, paramagnetic, ferromagnetic and anti-ferromagnetic.

By reducing the size of a ferromagnetic material, a critical size may be reached, on which only one domain can be sustained. This phenomenon is called superparamagnetism [2]. The magnetization curve of a material with this phenomenon resembles the ferromagnetic curve in a sense that it has a saturation magnetization, however, both the coercivity and remanence are zero, i.e., at zero applied field, the material is perfectly non-magnetic.

2.2. Magnetic Ink

Magnetic ink is no more than a fluid media with magnetic properties. The ink is usually made of mainly four types of ingredients [13]: the colorants, or magnetic pigments, which present the ink with color and the magnetic properties. They are usually magnetic nanoparticles of some ferromagnetic alloy; the vehicles or binders, which have multiple functions in the ink such as dispersing and binding the particles modifying the mechanical properties, and also presenting some other special properties; the solvent, which dissolves all the other components and adjusts the viscosity of the ink; and other additives which are specific for each ink and are designed to enhance properties of the ink.

Although real nanoparticles can have a complex magnetic structure, an assembly of noninteracting single-domain isotropic nanoparticles behaves like the above described superparamagnetism. At a temperature T in an applied field H, the average magnetization of the assembly is given by [8]:

$$
M = M_S \left[\coth \left(\frac{\mu_0 m_p H}{kT} \right) - \frac{kT}{\mu_0 m_p H} \right], \tag{3}
$$

where m_p is the individual magnetic moments of

the particles and k the Boltzmann's constant. This equation is a Langevin-like function.

2.3. Magnetic Tunnel Junctions

Magnetic Tunnel Junctions (MTJs) are structures based on the Tunnel Magnetoresistance (TMR), which is defined as the change in electrical resistance as a function of an external applied magnetic field. It is described by the equation

$$
\text{TMR} = \frac{R_{max} - R_{min}}{R_{min}},
$$

with R_{min} and R_{max} the minimum and the maximum electrical resistance, respectively [7]. MTJs are structures based on a multilayer structure with two ferromagnetic (FM) layers separated by an insulator (I), typically aluminum oxide (Al_2O_3) or magnesium oxide (MgO) [12], in a configuration FM-I-FM. One of the FM layers has a fixed magnetization and the other is free to rotate with the external magnetic field. When the FM layers have anti-parallel magnetization, the junction has its high resistance state. The low resistance for parallel direction magnetization. The ideal transfer curve of a TMR sensor is presented in Figure 1.
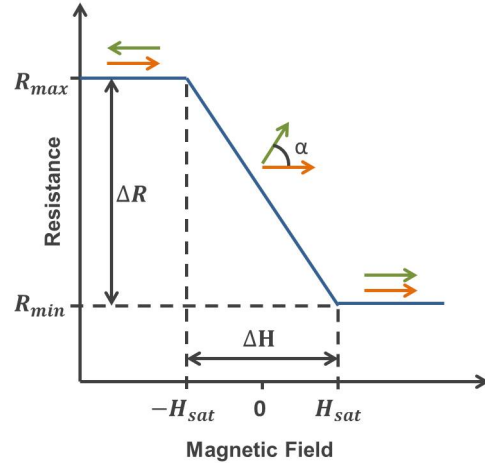

Figure 1: Ideal transfer curve of a MTJ sensor.

Using the physical factors obtained from the transfer curve, one can define the sensor field sensitivity, which is defined as the variation of the resistance (output) with respect to the magnetic field variation (input), or how reactive the sensor is to a field variation. For the ideal linear response, the MTJ sensor sensitivity S can be expressed by the slope o the linear region, normalized to its minimum resistance, taking into account the TMR ratio:

$$
S = \frac{1}{R_{min}} \left(\frac{\Delta R}{\Delta H} \right)_{linear} = \frac{\text{TMR}}{(\Delta H)_{linear}} \qquad [\%/Oe]. \tag{4}
$$

2

A sensor can achieve a high sensitivity by reducing the saturation fields and increasing the TMR ratio.

In the linear region of the sensor's response, the sensor resistance can be described as the sum of a nominal resistance R_0, at zero magnetic field, and a variation ΔR that, looking at equation 4 is directly related to the variation of the applied magnetic field (with zero magnetic field) H and the sensor sensitivity $S(V_b)$:

$$R(H) = R_0 + \Delta R = R_0 + S(V_b)R_{min}H \qquad (5)$$

Consequently, the voltage output variation ΔV due to an external magnetic field variation $\Delta H = H_2 - H_1$, and the current bias I that flows through the MTJ due to the bias voltage applied can be written as:

$$\Delta V = (R(H_2) - R(H_1))I = S(V_b)R_{min}I\Delta H \quad (6)$$

3. System Description and Characterization

The studied system is a magnetic encoder, therefore it has two main different units: the sensing head with the magnetic sensor alongside the integrated electronics; and a track, which encodes the information.

As an interdisciplinary project, the development has input from the different parts: the magnetic ink is provided by BOGEN Electronics GmbH[1], who is also responsible for printing the magnetic ink structures and developing the integrated electronics as well as the future casing and packaging; and INESC-MN is responsible for both the characterization of the ink and the development of the sensing head configuration for the system.

3.1. Configurations

To read the MI a constant magnetization of the patterns is needed to saturate its magnetization. The magnetization of the ink creates stray fields between the poles created on the structures. The magnetic sensor is able to measure these stray fields. The strategy to magnetize the ink in this work is to implement the magnets alongside the sensor on the reading head.

In total, six different configurations were considered. However, the requirements for the system left out all except for configuration standards Std_1 and Std_3 (Figures 2 and 3). These requirements are: a) the sensing head must be able to measure in both directions of movement, which is not met by Std_5 and Std_6; b) the sensor must be placed so that it can be as close as possible to the samples (bottom

[1]http://www.bogen-electronic.com/en/

of the sensing head); and c) the magnetic ink structures must be magnetized in-plane in order to create alternating poles in the direction of the movement, which is not met by Std_2 and Std_4.
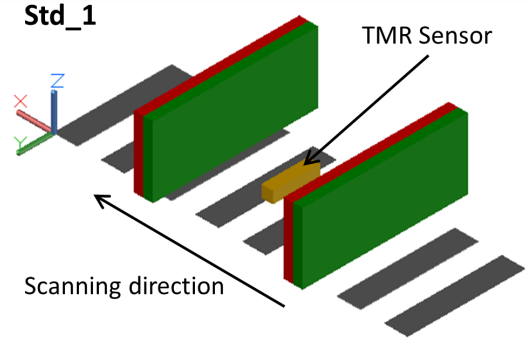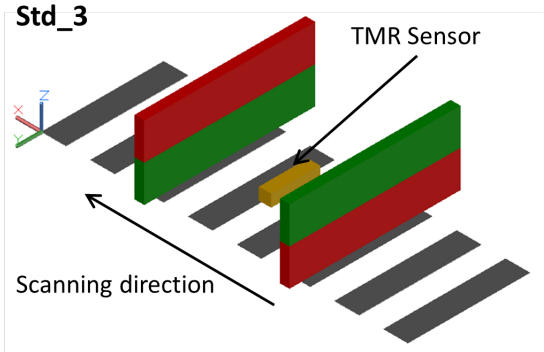

Figure 2: Std_1.

Figure 3: Std_3.

According to the two considered configurations, two different magnets were used. Both magnets have the same dimensions, and only the magnetization direction differs. The parameters are as follows:

Configuration	Geometry (mm^3)	μ_r	$\overrightarrow{B_r}$ (T)
Std_1	1×10×4	1.05	1.43 $\overrightarrow{e_x}$
Std_3	1×10×4	1.05	1.43 $\overrightarrow{e_z}$

Table 1: Physical parameters of the magnets used.

3.2. Simulations of the Magnets Configurations

Simulations were done on both configurations Std_1 and Std_3. In the configurations, one of the goals is to have minimum influence from the magnets' stray field on the sensor in order to maintain its high sensitivity characteristic. So, no field components on the sensitive plane $(y0z)$ of the sensor can be present.

Simulations on the magnetic field created by the magnets were done using the simulation software COMSOL Multiphysics 5.0. From the simulations of both configuration standards, it is evidenced a high variation of the z component of the field in the point where the sensor is placed. This leads to a requirement for very high precision in the placement of the sensor between the magnets.

Further simulations showed that for Std_3, placing the sensor 0.5 mm ($a = 0.5$ mm) below the base line of the magnets would greatly decrease the z component variation. In fact, where the sensor is placed, no variation from this component of the field happens.

3.3. Magnetic Sensor Characterization

In this work, two TMR sensors with different geometries were considered:

- **Sensor S1** is an array of 72 sensing elements (MTJs) with an individual area of 50×50 µm^2 distributed along 8 columns and 9 rows occupying a total area of 525×570 µm^2 to maximize the SNR [4];

- **Sensor S2** is an array of 4 sensing elements (MTJs) with an individual area of 10×4 µm^2 distributed along 4 columns and 1 row occupying a total area of 58.5×4 µm^2.

The MTJs on the two sensors have the same stack, which has a soft pinned sensing layer, with both a SAF and a SF. The stack is resented on Figure 4.
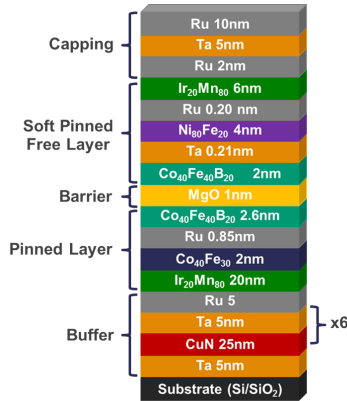

Figure 4: Thin film structure of the used MTJ pillar.

The magnetic behavior of both sensors was studied by measuring the transfer curve, making use of a magnetotrasport measuring tool. This tool makes a sweep of the field between -14 mT and 14 mT, and measures the resistance of the sensor. A bias current is applied in a CPP (current perpendicular to the plane) configuration: 100 µT for sensor S1 and 50 µT for sensor S2. The voltage measurement is done directly on the PCB with the mounted sensor.

The transfer curves were measured for the system with no magnets present and for both Std_1 and Std_3.

On Figure 5 the transfer curve measured for sensor S1 with Std_1 was measured. Notice the presence of the blue curve, taken as a reference, which is the transfer curve of the sensor with no magnets on the system.
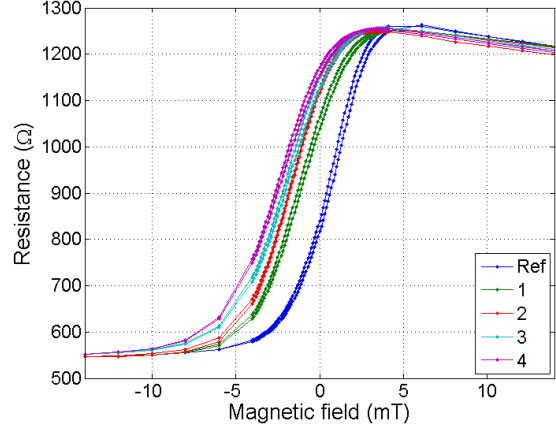

Figure 5: Set of transfer curves obtained for sensor S1 in a Std_1 configuration, alongside the reference curve.

As expected from the simulations previously made, the transfer curve on the Std_1 configuration is not easily reproducible. The configuration, and in specific the relative position between the magnets and sensor, is very sensitive to outer factors. Therefore, different curves were measured for different measurements, and the resulting parameters presented in Table 2. The effect of Std_1 on sensor S2 is usually just a shift of the linear region of the curve (the other parameters do not change significantly), which means that the influence is being made in the sensitive direction of the sensor, which is z, as it was expected from simulations.

	MR (%)	R_{min} (Ω)	S_0 (%/mT)	$\mu_0 H_f$ (mT)	$\mu_0 H_c$ (mT)
Ref	129	542	27.7	0.4	0.1
1	129 %	546	19.2	1.3	0.1
2	129 %	546	16.6	1.8	0.1
3	128 %	551	13.9	2.1	0.1
4	127 %	552	11.9	2.6	0.1

Table 2: Physical parameters derived from the transfer curves of sensor S1, without magnets and with configuration Std_1.

Sensor S2 was always saturated in a Std_1 configuration, due to its low area and thus being more prone to residual cross field from the magnets.

For Std_3, with $a = 0.5$ mm, the system is not so sensitive to changes in the positions, making the transfer curve reproducible, and for every measurement the same parameters were applicable, for sensor S1 and S2. Figures 6 and 7 show the curves alongside the reference curve for Std_3 using sensors S1 and S2 respectively. The important values for measurements derived from the transfer curves are presented on Table 3.
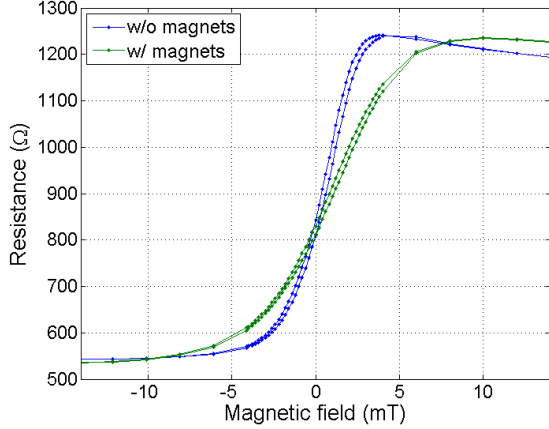

Figure 6: Sensor S1. $a = 0.5$ mm.

Std_3 has the effect of increasing the linear range of the curve of sensor S1, maintaining the TMR ratio, resulting in a lower sensitivity. This effect arises not from components in the sensing direction (z) of the sensor, but from components perpendicular to it, but still on the sensing plane of the sensor (y). The influence from this component was not expected on simulations, meaning that in the region where the sensor is located, the y component of the field is not zero.
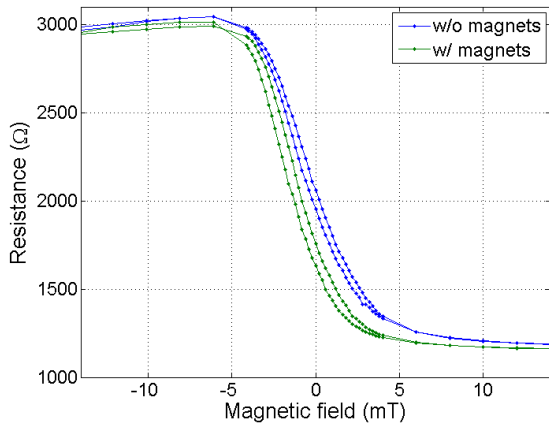

Figure 7: Sensor S2. $a = 0.5$ mm.

On sensor S2 however, the main effect is the shift of the curve, which arises from the influence of the z component of the cross field from the magnets. This shift has however, the effect of increasing the sensitivity.

	MR (%)	R_{min} (Ω)	S_0 (%/mT)	$\mu_0 H_f$ (mT)	$\mu_0 H_c$ (mT)
S1					
Ref	129	542	27.7	0.4	0.1
Std_3	131	542	14.3	0.8	0.1
S2					
Ref.	156	1187	-22.2	0.4	0.2
Std_3	159	1161	-24.4	1.3	0.3

Table 3: Physical parameters derived from the transfer curves of sensors S1 and S2, without magnets and with configuration Std_3 and $a = 0.5$ mm.

3.4. Magnetic Ink Characterization

The magnetic ink received from Bogen was also characterized through profilomenter and vibrating sample magnetometer techniques. It allows the evaluation of the magnetic properties and also the prediction of the MI structures behavior.

4. Hard Magnetic CoCrPt Structures

For validation of the sensor, hard ferromagnetic structures using micro-fabrication techniques are developed. The material used was a magnetic alloy composed of Cobalt Chromium and Platinum: CoCrPt. A simulation of the samples as well as some measurements are also performed. The geometry of the samples is represented in Figure 8, where the length of each structure and the separation is denominated as the pole-pitch, the width is always 3 mm and the thickness 1000 Å, and the substrate is glass. The samples vary in pole-pitch and number of structures N: 240 µm, 320 µm and 1000 µm with 35, 26 and 8 structures respectively.
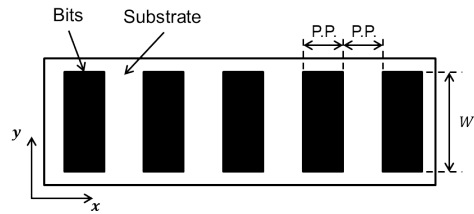

Figure 8: Structure of the micro-fabricated CoCrPt structures.

4.1. Micro-Fabrication

The micro-fabrication of the structures is done in four steps: alloy deposition, pole definition, excess material etching and finally setting of the magnetization.

The first step of the fabrication is the deposition on glass substrates of CoCrPt alloy, a magnetic alloy. This is done using sputter deposition, and in specific DC magnetron deposition using the tool Alcatel SCM450. Two samples were deposited. One calibration sample to confirm the deposition rate of 6.48 Å/min [11]. After being confirmed, the final sample for the process with thickness of 1000 Å was also deposited.

The second step is the first part of the transfer of the designed pattern to the film that was deposited. It is a lithography and it leaves protected by a photo-resist (PR) just the structures that will ultimately make up the structures.

The unprotected material resulting from the last step is then etched by ion milling, with an etch rate of 0.8 Å/s. The PR is then removed using a microstrip. At the end, only the desired structures of the magnetic alloy are left.

Finally, in this work the magnetization of the structures was set using a magnetic annealing with a temperature of 350°C for 2 hours and an applied field of 0.5 T. However, there was no need for temperature in this step. Being a magnetic alloy, only applying a strong field on the desired direction would result in the desired magnetization, as it was done before for the same material deposited in same conditions in [11].

After this last step, the hysteresis curve (magnetization vs. applied field) was taken using a VSM technique. Figure 9 shows the resulting curve and the derived physical properties.
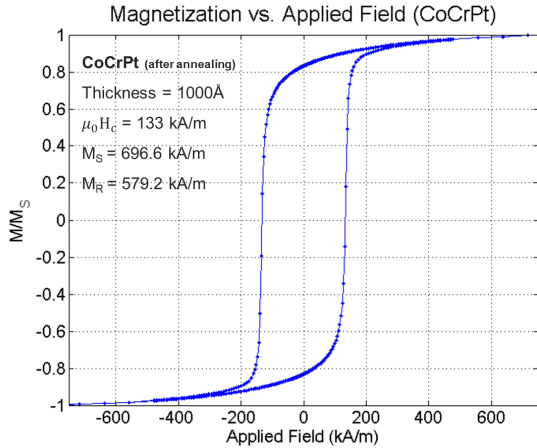

Figure 9: Hysteresis loop of magnetization vs. applied field for the deposited magnetic alloy CoCrPt.

4.2. Simulations

The simulations were done taking into account the characterization of the fabricated CoCrPt samples. In particular, taking the thickness and the saturation magnetization.

The simulation takes into account a 2D model of the structures and considers a uniformly magnetized media, with no currents. Taking into account the Coulomb approach to the magnetic field calculation, the 2D field created by superficial charges is given by the integral:

$$\mathbf{H}(\mathbf{r}) = \frac{1}{2\pi} \int_P dr' \left(\mathbf{M}(\mathbf{r}') \cdot \mathbf{e}_n \right) \frac{\mathbf{r} - \mathbf{r}'}{|\mathbf{r} - \mathbf{r}'|^2}, \qquad (7)$$

where $\mathbf{r} - \mathbf{r}'$ is the vector between a point in the magnetized material ($\mathbf{r}'$) and the point where the field is calculated ($\mathbf{r}$). And $\sigma_m = (\mathbf{M}(\mathbf{r}') \cdot \mathbf{e}_n)$ is the superficial charge density. For a plane surface (or a line in 2D), the integration of this equation becomes

$$H(r, \theta) = -\frac{\sigma_m}{2\pi} \left(\Delta\theta + i \log\left(\frac{r_2}{r_1} \right) \right) = H_n + iH_t, \qquad (8)$$

yielding a normal (H_n) and tangential (H_t) field to the magnetized surface. And being r_1 and r_2 the distances to the corners of the surface line, and $\Delta\theta$ the subtended angle.

For the CoCrPt structures, the surfaces of interest lie on the z axis, and since the sensors are sensitive on the z direction the tangential component is considered for the field calculation in the model. Let N denote the number of structures on the sample (and $k = 0, ..., (N-1)$ the index of the structure), t the thickness of the structures (in z) and pp the Pole Pitch length (in x). The magnetic field at any point $\mathbf{r} = (x, z)$ is calculated by summing the contributions from all structures, each having two charged surfaces with opposing charges:

$$H_z(x, z) = \frac{M_R}{2\pi} \sum_{k=0}^{N-1} \left(-\log \frac{r_2^k}{r_4^k} + \log \frac{r_1^k}{r_3^k} \right), \qquad (9)$$

being r_2^k and r_4^k the magnitudes of the vectors between the point of the calculated field and the corners of the positively charged surface; and r_1^k and r_3^k the magnitudes of the vectors between the point of the calculated field and the corners of the negatively charged surface. The corresponding vectors taking into account Figure 10, are given for any (x, z) by:

$$
\begin{aligned}
\mathbf{r}_1^k &= \left(x - 2k * pp, z - \frac{t}{2} \right), \\
\mathbf{r}_2^k &= \left(x - 2k * pp, z + \frac{t}{2} \right), \\
\mathbf{r}_3^k &= \left(x - pp - 2k * pp, z - \frac{t}{2} \right), \\
\mathbf{r}_4^k &= \left(x - pp - 2k * pp, z + \frac{t}{2} \right).
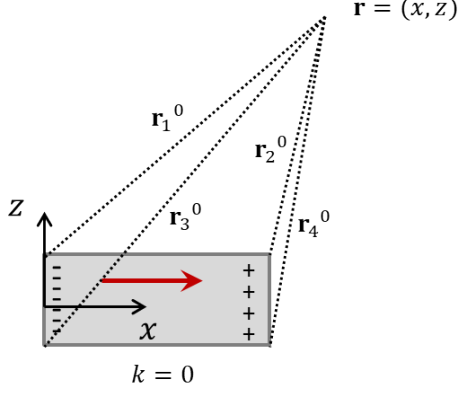\end{aligned}
\qquad (10)
$$

Figure 10: Scheme of the contributions to the calculation of the field of just one PM CoCrPt structure. The red arrow indicate the direction of the magnetization of the structure.

To perform the simulation, the software MATLAB is used. After the parameters such as the PP, RD, t and M_R defined, the program computes the vectors as given in 10 and applies the equation for the z component of the field 9.

5. Measurements

The measurement setup is composed of an XYZ automated scanner with a micrometric resolution. Some electronic instruments are also present to generate the required signals and to demodulate the sensor's output. For more information about the measurement system the reader can consult reference [6].

Each measurement performed in this work consisted on a magnetic scan over a a sample with magnetic structures, whether made with MI or CoCrPt, using the above described system. In specific for CoCrPt samples, the raw measurements were taken so that some values could be more accurately calculated. First, each scanning is done over an area where no magnetic signal is expected (where no magnetic bits are present), so to provide an accurate offset value (voltage at zero field), this area is taken 2 mm before the first structure on the x direction. The number of structures to be scanned was always chosen as to incorporate at least 6 consecutive poles. When only a curve is represented (and not the entire 2D scan), it is chosen as the center line of the scan, at $W/2$ where the field is expected to be stronger and more uniform. Figure 11 shows a scheme of the scanned areas and also the center line. Each measurement has also a specific resolution in x and y, which correspond the size of the step between consecutive measurements. The step in x is always smaller than the step in y, since the sought after behavior happens on the movement on x.
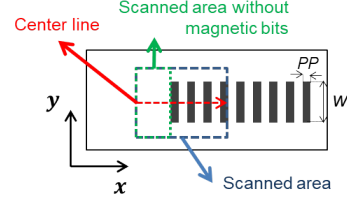

Figure 11: A scheme of the scanning measurements done on the different CoCrPt samples.

The uncertainty of the position in z was estimated to be of 14µm, due to the method of finding $z = 0$ and the resolution of the motor.

The voltage output from the setup is then converted to the magnetic amplitude by using the equation:

$$H = \frac{V - V_{off}}{RS_0 I_b}, \qquad (11)$$

where H is the magnetic field magnitude in mT, V the output voltage from the sensor in V, V_{off} the offset voltage of the measurement in V, R_{min} the minimum resistance in Ω, S_0 the sensitivity of the sensor in %/mT and I_b the bias current fed to the sensor in A.

5.1. Measurements on Magnetic Ink Samples

Measurements on MI samples with sensor S1 using both Std_1 and Std_3 allowed the evaluation of the best solution for the system. The use of Std_3 resulted in a higher effective magnetization of the ink during measurements, which was already expected with the simulations of the magnets configurations, due to the presence of the x component of the field in the region right below where the sensor is measuring. Using both configurations resulted also in similar spatial-resolutions, since the same sensor was used. However, the higher magnetization of the ink yields higher magnetic signal, thus more distinguishable measuremets using Std_3.

Sensor S2, which has a greater spatial resolution than sensor S1, was tested on the same samples and doing the same studies as with sensor S1. Sensor S2 resulted in higher spatial resolution, allowing the measurement of smaller structures. It measures also higher magnetic signals from the samples, due to its lower effective reading distance. However, this sensor has a lower SNR, resulting in worst performance reading smaller magnetic signals.

5.2. Sensor S1 Validation with CoCrPt Samples

The validation with sensor S1 was done using the micro-fabricated CoCrPt samples. The simulation of sensor S1 took into account the span of the sensor of 570 µm on the z axis, by doing an average of the field calculated over 10 points on this line. The

7

reading distance (RD) on the simulations is also a corrected RD, which is the nominal RD plus contribution from the uncertainty and the distance between the sensor itself and the bottom of the PCB.

The measurements were done on the three samples with a reading distance of half the pole pitch. The samples have pole-pitches of 240µm, 320µm and 1000µm.
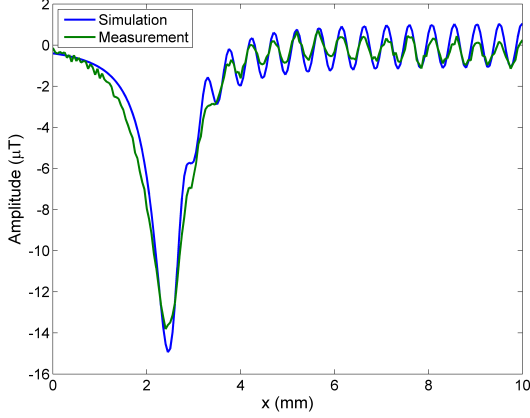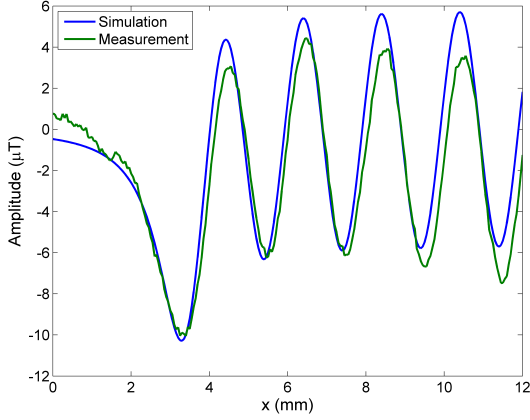

Figure 12: Sensor S1 in a Std_3 configuration. PP = 240 µm.

Figure 13: Sensor S1 in a Std_3 configuration. PP = 1000 µm.

Of each measurement and simulation, the denominated large and small average amplitudes are calculated. From a tendency comparison, such as in Figures 12 and 13, it is evidenced that the sensor is measuring in fact the field created by the magnetic structures. It is also seen on the measurement that some offset signal is measured, which is not constant, meaning that the measurements have some background field.

However, the amplitudes don't quite match with the expected values. The plot on Figure 14 shows the comparison between simulation and measurements. The large amplitude increases for smaller pole-pitch structures since we are putting the sensor gradually closer to the sample as the PP decreases, the small amplitude on the other end tends to decrease, this is due to the fact that the poles are getting closer together, closing the stray field force lines at a closer scale resulting in a gradually weaker z component of the field.
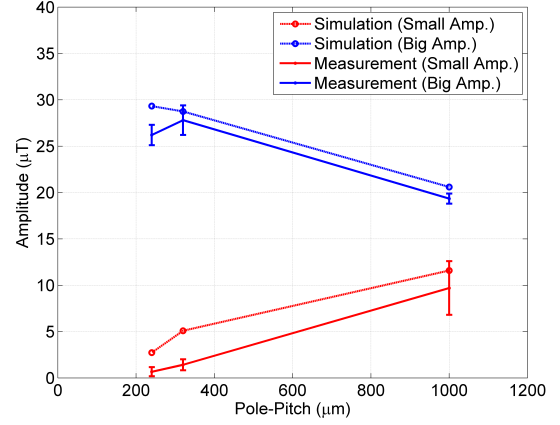

Figure 14: Average amplitudes measured both in the measurements and simulations for sensor S1 for each sample at a RD of half the PP.

The fact that the amplitudes don't match may come from different factors. First, an underestimation of the uncertainty in the RD of the measurements. 14 µm was considered as the uncertainty, however, this values may be higher, and if so, the difference between simulation and measurement could be explained. On the other hand, the model for the simulation is a 2D approximation, where an average is performed over the span of the sensor. This approximation may, however be faulty, and is not considering the full extent of the field variation along the sensor. Other factor may come from the model itself, since we are considering perfect magnetization uniformity within the material.

Due to the closeness in tendency of the measurements in relation to the simulation, one can say that sensor S1 is reliable, and makes reliable measurements in terms of magnetic signal form. Therefore, making reliable measurements on magnetic ink samples.

5.3. Sensor S2 Validation with CoCrPt Samples

For sensor S2 the simulation simplifies since the sensing region is much smaller, being of just 4µm. Therefore, the field calculated in the simulation for this sensor is done on just one point at the corrected RD, which is calculated as it was done in the previous section. The samples measured are the same as

the used for the validation of sensor S1. The measurements are also done at half the pole-pitch for each sample.
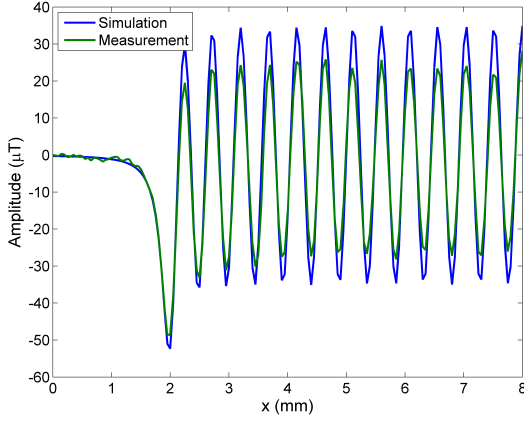

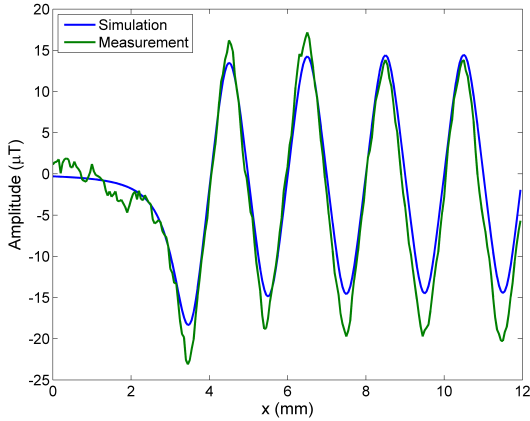Figure 15: Sensor S2 in a Std_3 configuration. PP = 240 µm.

Figure 16: Sensor S2 in a Std_3 configuration. PP = 1000 µm.

Of each measurement and simulation, the denominated large and small average amplitudes are calculated. From a tendency comparison, such as in Figure 15 and 16, it is evidenced that the sensor is measuring in fact the field created by the samples. In terms of the closeness of the amplitudes to the simulation, sensor S2 seems to have a better performance. It is noticed also that the magnetic signal read is higher than for sensor S1, due to the fact that since sensor S1 performs an average over its area, the effective reading distance is lower for sensor S2, however the measurements with sensor S2 show lower Signal-to-Noise Ratio (SNR).

A comparison is then performed between the different amplitudes measured on the samples, and simulated. On Figure 17 this comparison is shown.
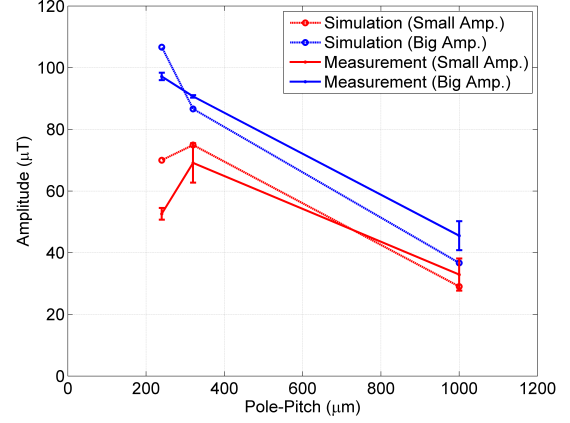

Figure 17: Amplitudes measured both in the measurements and simulations for sensor S2 for each sample at a RD of half the PP.

Overall the behavior predicted by the simulation is followed by the measurements, noticing in specific that the decrease in the small amplitude between the 320µm sample and 240µm also happens in the measurement, even if at a bigger scale. As already seen for sensor S1, the increase of the large amplitude as the pole-pitch decreases has to do with getting gradually closer to the sample. However, the predicted behavior for the small amplitude is different from the predicted behavior for sensor S1. It must be present here that sensor S1 is averaging over an area that spans 570µm over z, this results in an effective reading distance of the half pole-pitch plus around 200µm which is of 700µm for 1000µm PP, 360µm for 320µm PP and so on. While 200µm is just a relatively small fraction of 1000µm, it makes already a big portion of 320µm adn 240µm. Therefore, with sensor S2 the sensor is significantly closer to the sample, and so, the magnetic field from the smaller pole pitches is higher than for 1000µm sample. Then, comparing the lower PP sizes, the explanation given for sensor S1 holds, since the structures are much closer to each other, the stray field closes in a smaller scale, decreasing the signal.

Sensor S2, even though having a lower SNR, in a Std_3 configuration its sensitivity and spatial resolution are higher than for sensor S1. Resulting in a much better expected performance in terms of resolution for this sensor. This comes as a great advantage for reading magnetic ink. The closeness of the measurements to the simulations validates also this sensor, and the procedure used, making it a reliable sensor for reliable measurements.

6. Conclusions

The aim of this work has been to develop a reading head based on the TMR sensor technology for

reading magnetic ink patterns, in particular for positioning application. This system should be able to magnetize the ink as well as measure it with high accuracy and sensitivity.

From two considered configurations (Std_1 and Std_3), Std_3 has been proven to be the most efficient in magnetizing the magnetic ink through measurements of printed magnetic ink patterns, and so reading higher magnetic field signal. The magnets in the best configuration has also reduced influence on the sensors and thus allowing maintenance of a high sensitivity for measurements.

A strategy to validate the sensors was also developed, comprising on the micro-fabrication in a clean-room environment of well-defined structures of a CoCrPt hard ferromagnetic alloy. The simulation of this scales compared with measurements showed that the measurements for both sensors are reliable, and that their response is very close to the simulations, showing the same tendency on both sensors. Tendency apart, the values of the amplitude still didn't exactly correspond, showing the results of the approximations taken in the simulation performed. It was a 2D model, therefore leaving out some 3D geometrical features that would influence the signal. These measurements allowed as well a good comparison between the two sensors used. Even though having a lower SNR, sensor S2 is capable of measuring higher amplitudes and has a better spatial resolution than sensor S1.

With this work, we were therefore able to find a configuration with a very good performance in magnetizing the magnetic ink, as well as validating the state-of-the-art TMR sensors for this application. Furthermore, the foundations for a future development of the system has been set.

Future work in this project should include the optimization of the sensors for this configuration. Even though a high spatial resolution sensor was found, the SNR is still low, requiring some future improvement. The CoCrPT scales, which proved to be a good validation tool for the sensors can also be optimized by fabricating higher thicknesses of alloy and therefore measuring higher signals, making a more versatile tool for different kind of studies.

Acknowledgements

References

[1] BOGEN Electronic GmbH. Magnetic Measurement Technology. `http://www.bogen-electronic.com/en/magnetic-measurement-solutions/technology.html`. Accessed: 2017-08-28.

[2] C. Bean and u. D. Livingston. Superparamagnetism. *Journal of Applied Physics*, 30(4):S120–S129, 1959.

[3] H. N. Bertram. *Theory of magnetic recording*. Cambridge University Press, 1994.

[4] F. A. Cardoso, L. S. Rosado, F. Franco, R. Ferreira, E. Paz, S. F. Cardoso, P. M. Ramos, M. Piedade, and P. J. Freitas. Improved magnetic tunnel junctions design for the detection of superficial defects by eddy currents testing. *IEEE Transactions on Magnetics*, 50(11):1–4, 2014.

[5] J. M. Coey. *Magnetism and magnetic materials*, chapter 2, pages 24–61. Cambridge University Press, 2010.

[6] F. Franco, F. A. Cardoso, L. S. Rosado, R. Ferreira, S. Cardoso, M. Piedade, and P. P. Freitas. Advanced ndt inspection tools for titanium surfaces based on high-performance magnetoresistive sensors. *IEEE Transactions on Magnetics*, 53(4):1–5, 2017.

[7] P. Freitas, R. Ferreira, S. Cardoso, and F. Cardoso. Magnetoresistive sensors. *Journal of Physics: Condensed Matter*, 19(16):165221, 2007.

[8] S. P. Gubin. *Magnetic nanoparticles*. John Wiley & Sons, 2009.

[9] D. C. Leitao, E. Paz, A. V. Silva, A. Moskaltsova, S. Knudde, F. L. Deepak, R. Ferreira, S. Cardoso, and P. P. Freitas. Nanoscale magnetic tunnel junction sensing devices with soft pinned sensing layer and low aspect ratio. *IEEE Transactions on Magnetics*, 50(11):1–8, 2014.

[10] S. Tumanski. Magnetic sensors. In *Handbook of magnetic measurements*, pages 159–256. CRC Press, 2016.

[11] J. P. D. Valadeiro. Magnetoresistive sensors with pico-tesla sensitivities. Master's thesis, Instituto Superior Técnico, September 2014.

[12] S. Yuasa and D. Djayaprawira. Giant tunnel magnetoresistance in magnetic tunnel junctions with a crystalline mgo (0 0 1) barrier. *Journal of Physics D: Applied Physics*, 40(21):R337, 2007.

[13] X. Zhou, C. Fang, Y. Li, N. An, and W. Lei. Preparation and characterization of fe 3 o 4-cnts magnetic nanocomposites for potential application in functional magnetic printing ink. *Composites Part B: Engineering*, 89:295–302, 2016.